Microstructure and texture evolutions in FeCrAl cladding tube during pilger processing

Available online at www.sciencedirect.com

jmr&t Journal of Materials Research and Technology

journal homepage: www.elsevier.com/locate/jmrt

Microstructure and texture evolutions in FeCrAl cladding tube during pilger processing

Xiao Qin [a,b], Ruiqian Zhang [c], Peinan Du [c], Jingyuan Pei [c], Qianfu Pan [c], Yu Cao [b], Huiqun Liu [a,*]

[a] School of Materials Science and Engineering, Central South University, Changsha, 410083, PR China
[b] Department of Industrial and Materials Science, Chalmers University of Technology, Gothenburg, 41296, Sweden
[c] Science and Technology on Reactor Fuel and Materials Laboratory, Nuclear Power Institute of China, Chengdu, Sichuan, 610213, PR China

ARTICLE INFO

Article history:
Received 10 May 2023
Accepted 27 June 2023
Available online 29 June 2023

Keywords:
FeCrAl cladding tube
Laves precipitate
Microstructure
Texture
Pilger

ABSTRACT

The microstructure of FeCrAl cladding tubes depends on the fabricating process history. In this study, the microstructural characteristics of wrought FeCrAl alloys during industrial pilger processing into thin-walled tubes were investigated. The hot extruded tube showed ~100 μm equiaxed grains with weak α*-fiber in {h11}<1/h12> texture, while pilger rolling process change the microstructure to fragmented and elongated grains along the rolling direction. The pilgered textures could be predicted with the VPSC model. The inter-pass annealing at 800–850 °C for 1 h results in recovery and recrystallization of the ferric matrix and restoration of ductility. The final finished tube shows fine recrystallized grains (~11 μm) with dominant γ-fiber in three dimensions. Pilger rolling enhanced α-fiber while annealing reduced α-fiber and enhanced γ-fiber. Microstructural evolution in the Laves precipitates followed the sequence of faceted needle-like → spherical → faceted ellipsoidal. Thermomechanical processing resulted in cladding tubes with an area fraction of ~5% and a number density of 5×10^{-11} m^{-2} in Laves precipitates, which is half that of the first-pilgered tube. Laves precipitates pin the grain boundaries to control the microstructure and prevent grain coarsening.

1. Introduction

FeCrAl alloys are increasingly being recognized as accident-tolerant fuel (ATF) cladding candidates for application in advanced Light-water reactors (LWRs) [1–3]. In a loss-of-coolant accident, the rapid increase in fuel temperature causes commercial zirconium alloy fuel cladding to be susceptible to severe degradation in high-temperature (>1200 °C) steam environments [4,5]. Unlike zirconium alloys, FeCrAl alloys exhibit excellent steam oxidation resistance [6–8], providing a large safety margin for the operation of nuclear reactors.

The manufacturing process of the cladding tube includes hot extrusion, reduction and annealing. Hot extrusion is usually performed at the recrystallization temperature to obtain the mother tube in preparation for subsequent reduction. The reduction typically involves a series of 3–5 passes in a rolling mill used to reduce simultaneously the diameter and wall thickness of tubes. The inter-pass annealing restores ductility and a final recrystallized annealing to achieve final

* Corresponding author.
E-mail address: liuhuiqun@csu.edu.cn (H. Liu).
https://doi.org/10.1016/j.jmrt.2023.06.255

Table 1 – Chemical composition of FeCrAl alloy tube (wt%).

Element	Cr	Al	Mo	Nb	Ti	Zr	Si	C	N	Fe
Content	12.5	3.8	1.8	0.98	0.19	0.02	0.23	0.003	0.002	Balance

mechanical properties and microstructural characteristics [9,10]. The fuel cladding in the LWRs requires a thin-walled seamless tube with a length of about 4 m, an outer diameter of about 10 mm and a wall thickness of less than 0.5 mm [9,11]. However, FeCrAl alloys have a single bcc structure and poor ductility due to the addition of Cr and Al [11–13]. These facts impose considerable challenges to fabricating tubes from FeCrAl alloys. Commercial FeCrAl alloy cladding development is still under laboratory conditions. The FeCrAl alloy cladding tube prepared by Yamamoto et al. [14,15] has problems with coarse grain and low dimensional accuracy. In addition, they found that the internal stress accumulated during the fabrication process caused the tube to fracture prematurely. Hence, it is essential to have an efficient processing flowsheet that results in cladding tubes with suitable microstructure, leading to optimized properties with required dimensional tolerances.

Pilger rolling has the advantages of large area reduction (up to 70–90% in a single pass), high production rate (up to 6 m/min for stainless steel), narrow dimensional tolerances, high surface quality and enhanced grain structure [16,17]. Pilger rolling for producing cladding tubes would be the way forward to obtain the required dimensional tolerances and optimized microstructure. Targeting the poor ductility of FeCrAl alloys, the warm pilger step aims to introduce a high level of substructure and improve formability. Cold pilger rolling could control the dimensional accuracy while annealing optimizes the final microstructure of the cladding.

Previous studies [18–20] have mainly focused on the microstructure and properties of FeCrAl plates, while little has been done to systematically investigate the microstructure of industrially fabricated FeCrAl cladding tubes, although they are crucial for the development of commercial cladding. The microstructure such as grain morphology, grain size, texture, nature and distribution of precipitate mainly depends on the thermomechanical processing (TMP) process [12–15,20–22]. Such microstructural aspects greatly influence strength, creep, precipitation and thermal stability, etc. [23–28]. The precipitates phase in FeCrAl alloys is C14-type Laves precipitate which was reported in previous studies [29,30]. Laves precipitates play a crucial role in controlling the microstructure and thermal stability of FeCrAl alloys [28,31,32]. Therefore, understanding the microstructure, texture, and precipitated phases of FeCrAl alloy cladding tubes in relation to TMP is important for the development of advanced cladding.

In this paper, FeCrAl alloy cladding tubes were fabricated by industrial hot extrusion (HE) and warm/cold-pilger rolling. EBSD and SEM were used to characterize the grain, Laves precipitate and texture of FeCrAl cladding tubes. The investigation could help us to better understand the limiting parameters of pilgering process and assess robust and reliable industrial pilger rolling of FeCrAl cladding tubes.

2. Experimental

The FeCrAl alloy used in the study was provided by Nuclear Power Institute of China. The chemical composition was analyzed by inductively coupled plasma optical emission spectrometer (ICP-OES), as shown in Table 1. The as-received FeCrAl hot-extruded tube was subjected to two warm pilger passes and three cold pilger passes with recovery anneals between each pilger step to produce the finished product tube. The TMP flow sheet of the FeCrAl cladding tube was shown in Fig. 1. We selected samples at typical conditions including as-extruded, as-pilgered and as-annealed for investigating the evolution of microstructure and texture. To facilitate

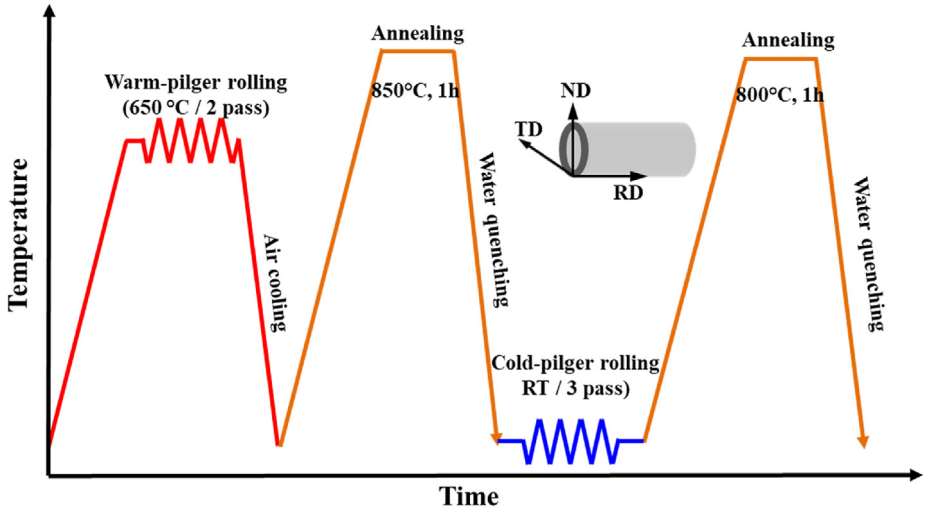

Fig. 1 – Processing route for the pilgering of FeCrAl alloy thin-walled tubes.

Table 2 – Tube dimension obtained during pilgering.

Step	Diameter (mm)	Thickness (mm)	Elongation (%)	Reduction (%)	Total strain	Q factor
HE	58.0	6.0	–	–	–	–
WR1	45.0	3.5	215	53	0.53	1.86
WR2	32.0	3.0	167	40	0.72	0.49
CR1	19.0	1.5	331	70	0.92	1.23
CR2	12.7	0.8	280	64	0.97	1.41
CR3	9.5	0.35	292	66	0.99	2.23

discussion in the following text, HE, WR1, CR1 and CR3An, etc. Represented hot-extruded, first warm-pilger, first cold-pilger rolling and third cold-pilger rolling annealing, respectively. The dimensions of the as-received hot-extruded tube and after each pilgered step tube were given in Table 2. The strain tensor generated during each pilgering step was obtained from the dimension evolution of pilgered tubes. The total strain is based on the per-pass strain superposition. Q factor represents the ratio of wall thickness reduction to diameter reduction for the corresponding pilgering step. RD, TD and ND corresponded respectively to axial, circumferential and radial directions of the tubes.

Electron backscatter diffraction (EBSD) data were collected using a JEOL JSM-7900F scanning electron microscope (SEM) coupled with an Oxford C-nano EBSD detector. Samples preparation for EBSD were done by grinding and polishing with silica colloidal oxide polishing suspension (OPS). The scanning step size varied from 1 to 8 μm depending on the processing conditions of tubes. To attain EBSD data, HKL* Channel 5 software was used for different analyses of inverse pole figure (IPF), grain boundary (GB), recrystallization fraction (REX), image quality (IQ) map, and orientation distribution functions (ODF) and grain size measurement. The average grain size was obtained by the linear intercept method and the grain reconstruction method, respectively. Table 3 lists the average grain size of the hot-extruded tube and subsequent processed tube samples. Grain boundary with misorientation larger than 15° were superimposed in the IPF maps as black lines. In the GB maps, boundary with misorientation lower and higher than 15° are separated into low angle grain boundaries (LAGBs) and high angle grain boundaries (HAGBs), respectively. The lower bound for LAGBs was selected to be 2° according to the angular resolution limit of the EBSD technique. The microstructure and distribution of Laves precipitates were characterized by combined use of backscattered electron (BSE) imaging and electron channeling contrast imaging (ECCI) in a TESCAN MIRA3 FE-SEM. The accelerating voltage is set at 20 kV and the working distance is about 15.1 mm. Image-Pro Plus software was used to determine the surface area fraction and number density of the Laves precipitates. Vickers hardness was measured on a longitudinal (RD-ND) plane using an HVS-1000 Micro Hardness Tester with a load of 1 kgf and 10 s dwell time. The average Vickers hardness values were calculated by measuring seven different locations. Room-temperature tensile tests of selected samples were performed with a nominal strain rate of 10^{-3} s^{-1}. Tensile specimens with a gauge length of 30 mm were machined using electric discharge machining with the tensile axis parallel to the RD.

3. Texture simulations

Texture predictions are obtained from polycrystal plasticity simulations performed using visco-plastic self-consistent (VPSC) model [33]. The VPSC algorithm considers each grain as a visco-plastic inhomogeneity within a homogeneous and anisotropic material. The VPSC model uses rate-dependent visco-plastic laws to correlate the macroscopic deformation behavior of polycrystalline materials with the microscopic deformation behavior (via slip and/or twins). Detailed descriptions of the VPSC model formulas and related model parameters can be found elsewhere [34].

The simulation in this study was performed in VPSC7d code and ATEX tools. First, the true stress-strain curves and EBSD results of the initial FeCrAl tubes were obtained based on experiments. Then the velocity gradient matrix and initial texture file are imported into VPSC7d. Modify the single crystal file to obtain the equivalent stress-strain curve consistent with the experimentally measured stress-strain curve. Finally, Run the VPSC program and import the texture output file into ATEX to plot the texture.

Unlike simple uniaxial tension, compression and planar rolling, the deformations that pilgering imposes on a typical

Table 3 – Measurement of grain size at different processing conditions.

Processed sample	Intercept length method			Grain reconstruction method		
	RD(μm)	TD(μm)	ND(μm)	RD-ND(μm)	TD-ND(μm)	RD-TD(μm)
HE	83.5 ± 50.6	82.2 ± 47.6	77.8 ± 44.7	94.1 ± 47.0	101.1 ± 54.6	–
WR2	43.9 ± 30.9	19.8 ± 15.5	25.0 ± 18.7	58.6 ± 31.1	34.1 ± 21.8	–
WR2An	22.3 ± 16.4	10.2 ± 10.3	12.2 ± 10.5	19.3 ± 12.4	17.9 ± 13.7	–
CR1	12.9 ± 9.8	8.0 ± 5.6	10.4 ± 8.9	17.3 ± 10.8	14.9 ± 9.9	–
CR1An	12.3 ± 8.1	11.5 ± 6.6	13.6±7.2	18.6 ± 9.3	16.6 ± 7.3	–
CR3An	8.9 ± 3.5	8.1 ± 2.3	9.3 ± 3.0	11.4 ± 4.8	11.4 ± 3.6	11.8 ± 3.5

material point in the tube are non-axisymmetric, unstable, and dependent on the location of the material point. Let $v_i(x_k)$ denote the material flow velocity at spatial coordinate x_k.

$$L_{ij}(x_k) = \frac{\partial v_i}{\partial x_k} \qquad i,j \in \{RD, TD, ND\} \tag{1}$$

Therefore, the velocity gradient matrix in the RD−TD−ND system is taken to be

$$[L]_{RD-TD-ND} = \begin{bmatrix} L_{RD,RD} & L_{RD,TD} & L_{RD,ND} \\ L_{TD,RD} & L_{TD,TD} & L_{TD,ND} \\ L_{ND,RD} & L_{ND,TD} & L_{ND,ND} \end{bmatrix} \tag{2}$$

Assuming the mandrel is rigid, continued contact between the groove and the mandrel.

$$\frac{\partial v_{ND}}{\partial x_{RD}} = L_{ND,RD} = 0 \tag{3}$$

$$\frac{\partial v_{ND}}{\partial x_{TD}} = L_{ND,TD} = 0 \tag{4}$$

Pilgering simultaneously reduces the diameter and thickness of the tube. The simplified model assumes a linear decrease in both diameter and thickness and requires conservation of volume during plastic deformation for tube yielding.

$$\frac{\partial v_{ND}}{\partial x_{ND}} = L_{ND,ND} = \frac{-q}{1+q} \tag{5}$$

$$\frac{\partial v_{TD}}{\partial x_{TD}} = L_{TD,TD} = \frac{-1}{1+q} \tag{6}$$

And

$$\frac{\partial v_{RD}}{\partial x_{RD}} = L_{RD,RD} = 1 \tag{7}$$

The value of q depends on the location of the material point before and after the pilgering process.

Let D and d denote the outer diameter of tube measured before and after pilgering. T and t are the wall thicknesses of the initial tube and final tube.

$$Q = \ln\frac{t}{T} \Big/ \ln\frac{d}{D} \tag{8}$$

$Q \gg 1$ implies that the deformation is dominant by diameter reduction. On the other hand, $Q \ll 1$ indicates deformation is dominated by the reduction in wall thickness. $Q \approx 1$ indicates deformation conditions similar to uniaxial extension along RD.

Consider the effective component of the velocity gradient.

$$L_{TD,ND} = L_{RD,TD} = L_{TD,RD} = L_{RD,TD} = 0 \tag{9}$$

4. Results

4.1. As-extruded microstructure

The microstructure and texture of the hot-extruded tube are shown in Fig. 2. In the IPF map, the longitudinal plane (Fig. 2(a)) and cross-sectional plane (Fig. 2(b)) consisted of equiaxed grains with different orientations. The grains with almost isotropic morphology in different directions indicate that the extruded microstructure is homogeneous. The average grain size in Table 3 is ~100 μm with an aspect ratio of 1.01 (RD compared to TD). The grain boundary map (Fig. 2(c)) shows that many grains are bordered by HAGBs in black color with a high fraction of ~84%. The main part of the recrystallization fraction map (Fig. 2(d)) includes dominant recrystallized grains by the blue region together with some substructured grains. These results indicate that the hot extruded tube almost completely recrystallized. The related ODF (Fig. 2(e)) at $\varphi_2 = 45°$ shows dominant α*-fiber ({h11}<1/h12>), λ-fiber (<001>//ND) and weak γ-fiber textures have been established in hot-extruded microstructure with the

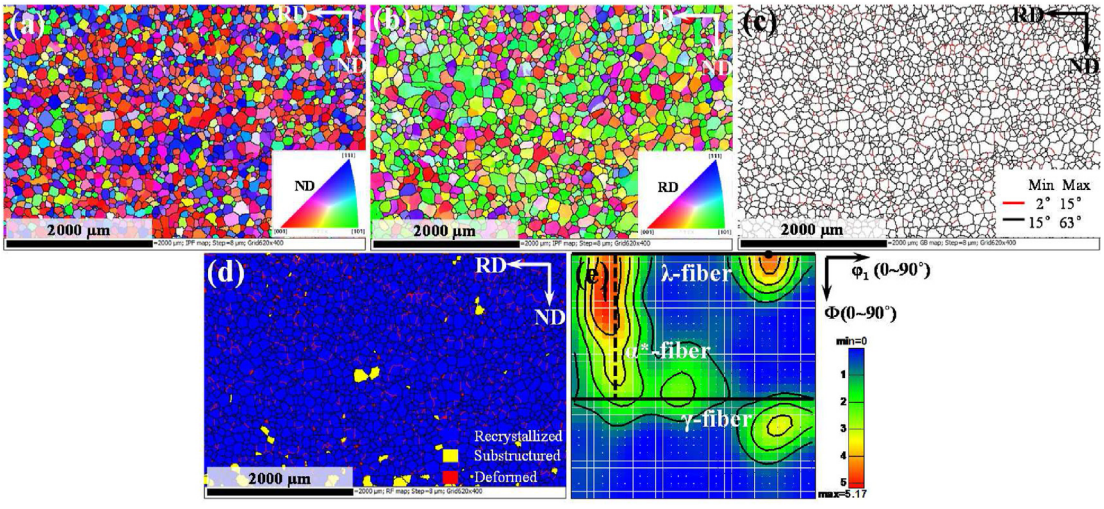

Fig. 2 – Microstructure and texture of the hot extruded FeCrAl tube including a) IPF map (RD-ND), b) IPF map (TD-ND), c) GB map, d) REX map, and e) ODF at $\varphi_2 = 45°$.

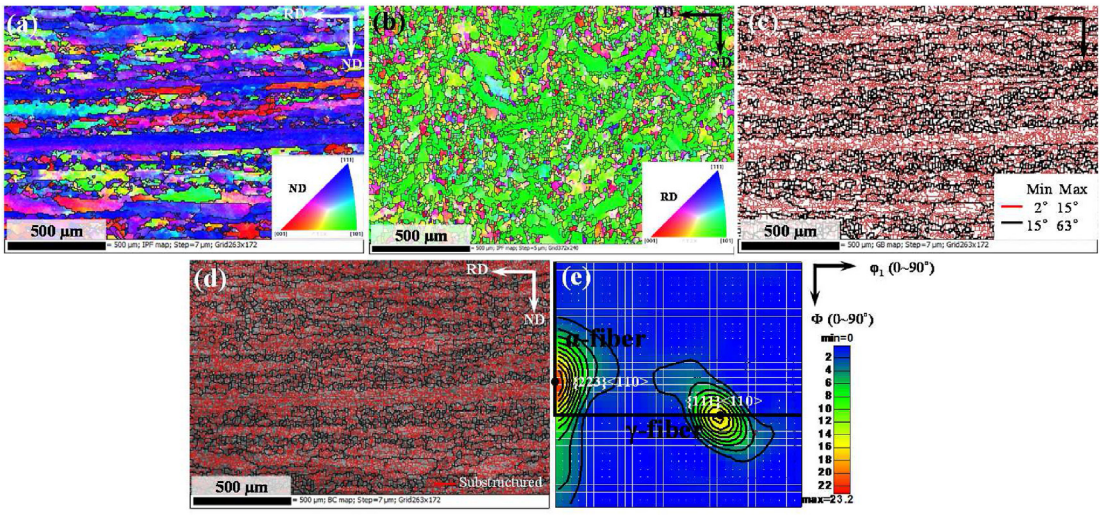

Fig. 3 – Microstructure and texture of 2nd warm pilgered FeCrAl tube including a) IPF map (RD-ND), b) IPF map (TD-ND), c) GB map (RD-ND), d) IQ map (RD-ND), e) ODF at $\varphi_2 = 45^\circ$.

main planes of {001}, {110} and {111} distinguished by red, green and blue grains in the related IPF map, respectively. Compared to the texture after hot extrusion in FeCrAl ODS alloys [35], the main difference is the appearance of the shift of the α-fiber towards the α*-fiber. The strong partial λ-fiber texture component was {001}<120>, while α*-fiber spread in whole orientations.

4.2. *As-pilgered microstructure*

Figs. 3 and 4 show the microstructure and texture evolution of the hot-extruded tube after 2nd warm-pilger and 1st cold-pilger rolling, respectively. In both figures, the IPF maps have been evaluated for two different sections including longitudinal plane (RD-ND) (Fig. 3(a) and 4(a)) and cross-section plane (TD-ND) (Fig. 3(b) and 4(b)). In the longitudinal plane, a lot of 'heterogeneous deformation' microstructure appeared, the grains are fragmented (i.e., formation of high-angle boundaries) and mainly elongated in addition to some equiaxed grains. The elongated grains along the RD with a width of ~60–100 μm. However, in the cross-section plane, torsional deformed grains with <110> orientation (green) can be observed in most regions. It can be rationalized by the fact that pilger rolling could introduce a significant shear component [36]. The comparison of average grain size in the RD and TD directions (Table 3) indicates a lower aspect ratio of grains in the rolling direction and smaller grain size of CR1 than WR2. The GB map (Fig. 3(c) and 4(c)) of longitudinal plane demonstrates that the grain structure changes to a mixture of fragmented and elongated grains. It is worth noting that there are many equiaxed sub-grains and grains in the <111> oriented grains engaged among or inside grains, including a high proportion of 51%–68% LAGBs as shown by red lines. In some cases, the size of elongated grains reached a few millimeters.

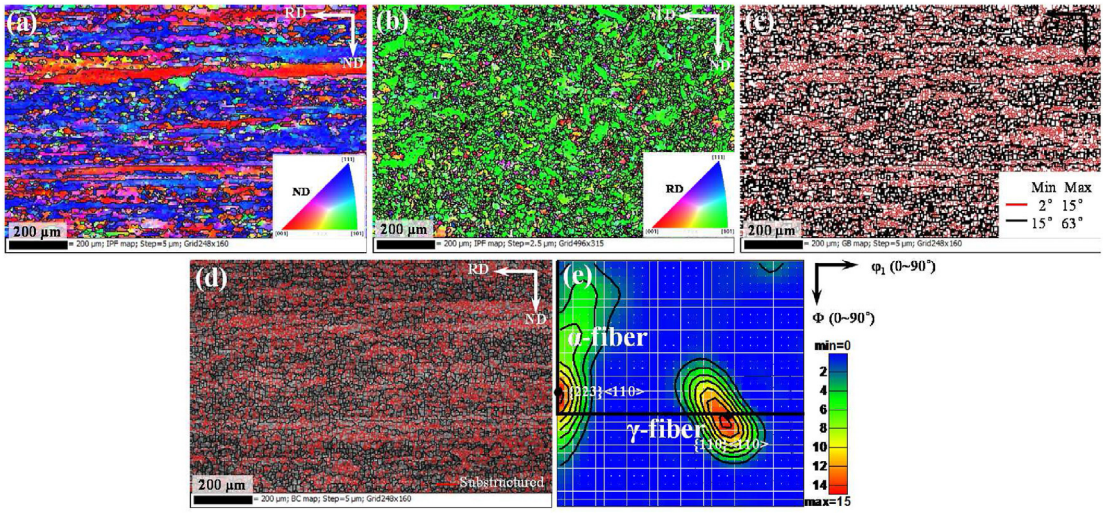

Fig. 4 – Microstructure and texture of 1st cold pilgered FeCrAl tube including a) IPF map (RD-ND), b) IPF map (TD-ND), c) GB map (RD-ND), d) IQ map (RD-ND), e) ODF at $\varphi_2 = 45^\circ$.

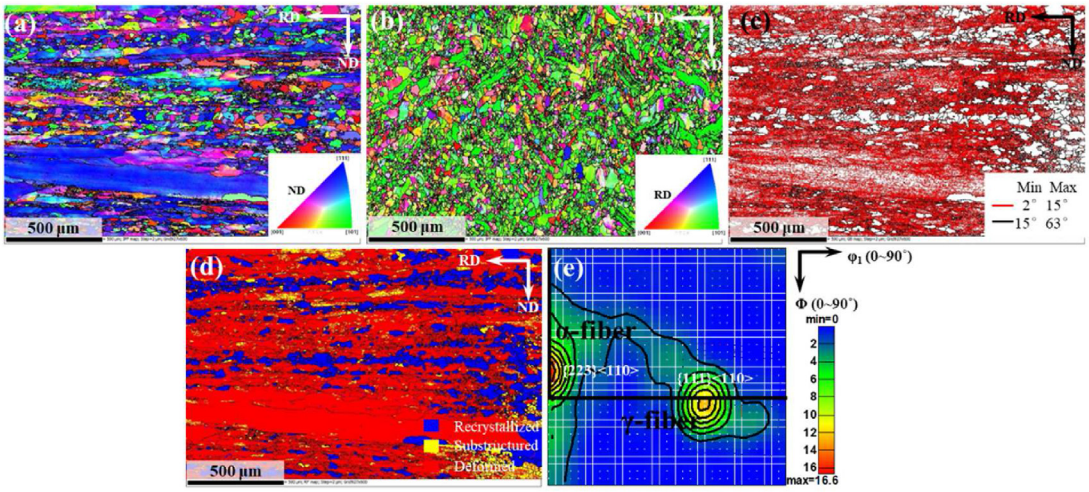

Fig. 5 – Microstructure and texture of annealed FeCrAl tube at 850 °C following 2nd warm pilgering including (a) IPF map (RD-ND), b) IPF map (TD-ND), c) GB map (RD-ND), d) REX map (RD-ND), e) ODF at $\varphi_2 = 45°$.

The related IQ maps (Figs. 3(d) and 4(d)) show that some parts of elongated grains have a seriously deformed structure, indicating a high stored energy accumulation which is characterized by {111} plane. The stored energy of the deformed grains depends on the orientation, ranging from {100}, {111} to {110} higher orders, respectively [37]. (e.g. {111} grain in Fig. 3(a) and {001} grain in Fig. 4(a)). The crystallographic textures of both WR2 and CR1 samples are presented in Fig. 3(e) and 4 (e)) show almost similar texture. The overall texture intensity of the CR1 sample is less than that of the WR2 sample, but the α-fibers spread in whole orientations. It illustrates a major change after pilger rolling as an extension in α-fiber with the invariant direction of <110>. As noticed in IPF figures, the pink grains of {001} <120> orientation observed in the hot-extruded condition completely disappeared and an abundant texture of new orientation of {223} <110> and {111} <110> can be seen.

4.3. *As-annealed microstructure*

To facilitate thin-walled tube production and prevent premature failure during the subsequent rolling process, intermediate anneals were carried out at 800–850 °C for 1 h. Fig. 5 presents the microstructure and texture of annealed tube after the 2nd warm pilger rolling. The microstructure of the WR2An tube in both longitudinal and cross-section planes show a bimodal structure (Fig. 5(a and b)). The bimodal structure in the longitudinal plane is mainly composed of elongated large grains with <111> orientation and ~10 μm recrystallized grains. The microstructure of the cross-section shows that mixed grains consist of equiaxed grains and <110> orientation strip grains. As shown in the grain boundary map (Fig. 5(c)), the deformed grains include a high-level density of LAGBs with a fraction of ~90%, which is consistent with the almost 67.1% deformed regions in the recrystallized fraction map (Fig. 5(d)). It is worth noting that after annealing at 850 °C for 1 h, there are still many deformed microstructures, which can be explained from the small area reduction and Q value in Table 2. The related ODF map shows strong α-fiber as in the as-pilgered condition.

The annealed 3rd cold pilger rolling tube had a significantly different microstructure and texture to that of annealed the 2nd warm pilger rolling tube. As observed in the IPF maps of the annealed tube in different sections (Fig. 6(a, b, c)), slightly elongated large grains with both typical blue and green grains with a length of ~11 μm at ~ 30° to the rolling direction or parallel the normal direction in addition to some finer equiaxed grains. The average grain size of the longitudinal plane, rolling plane and cross-section plane was 11.4 μm, 11.8 μm and 11.4, respectively. Both the low fraction of LAGBs about 8.8% (Fig. 6(d)) and the high recrystallized area fraction (Fig. 6(e)) indicate that almost complete recrystallization happened. The related texture in ODF (Fig. 6(f)) shows that two main α-fibers and γ-fibers have been developed which can be seen in the IPF maps as blue and green grains, respectively. The dominant γ-fiber indicates that recrystallization significantly reduces the rolling texture intensity and changes grains orientation.

4.4. *Laves precipitate distribution*

Laves precipitate distribution in the microstructure of both longitudinal and cross-section planes with different process steps was investigated by SEM. Fig. 7 shows the BSE images of Laves precipitate distributions indicated by the white contrast compared to the dark matrix. Previous studies have shown that these Laves phase particles were mainly $(Fe,Cr)_2(Mo,Nb)$ [28–30]. The faceted needle-like Laves precipitates were distributed at grain boundaries and within grains of the hot-extruded tube as shown in Fig. 7(a,e). After the first warm-pilger rolling, the morphology Laves precipitates changed from needle-like to spherical or elliptical, which was significantly different from the hot extruded state. Some cracks within Laves phase particles and deboning of the interface between the matrix and the Laves phase were occasionally observed, as marked by black arrows in Fig. 7(b). In the CR1 sample (Fig. 7c), Laves phase particles within shear deformed bands were observed to deviate from RD by ~15–35°. Fig. 7(b–h) shows that the Laves phase particles were

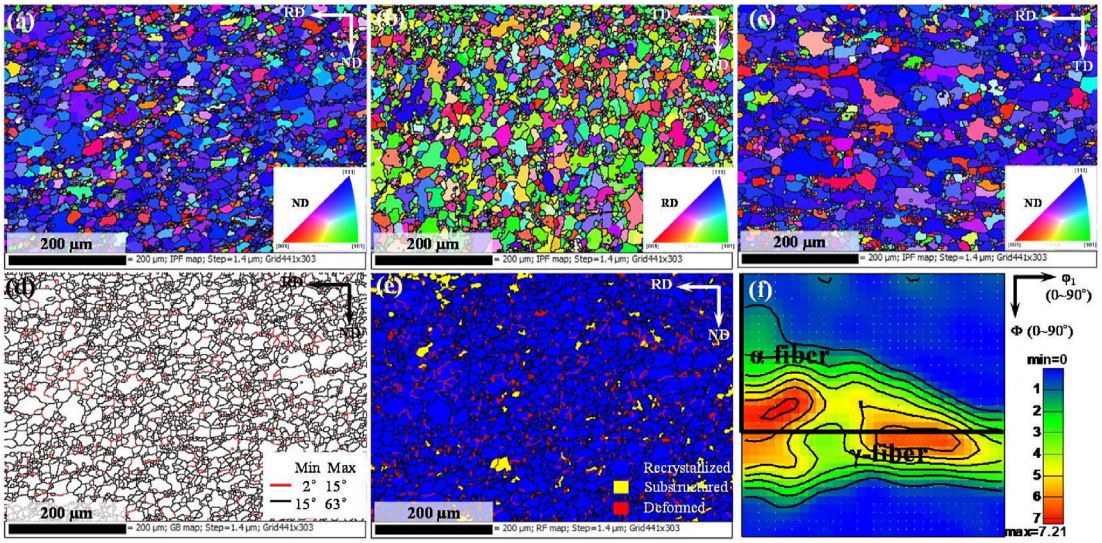

Fig. 6 – Microstructure and texture of recrystallized FeCrAl cladding tube at 800 °C following 5th cold pilgering including (a) IPF map (RD-ND), b) IPF map (TD-ND), c) IPF map (RD-TD), d) GB map (RD-ND), e) REX map (RD-ND), f) ODF at $\varphi_2 = 45°$.

homogeneously distributed in the matrix. Fig. 7(d,h) show that annealing results in coarsening of the Laves phase particles compared to the pilgered samples. The size statistics of Laves phase particles were summarized based on Image-Pro Plus as shown in Table 4. The results show that the distribution of Laves is homogeneous in both longitudinal and cross-section planes of the FeCrAl tube. During pilger processing of FeCrAl cladding tubes, the high number density and area fraction of Laves phase particles decreases from ~8 × 10^{11} m^{-2}, ~8% for WR1 tube (about two times) to ~4 × 10^{11} m^{-2}, ~4% for finished tubes, respectively. Laves phase particles were ~250 nm in the as-pilgered sample, while the coarsened Laves phase particles in the annealed sample were ~330 nm. The decrease in area fraction and number density indicates that applied TMP dissolves some of the Laves phase particles into the matrix. These finely dispersed Laves phase particles are important for controlling the microstructure and recrystallization of cladding tubes [28,31].

4.5. *Hardness and tensile properties*

Hardness is one of the methods to evaluate the mechanical properties of materials, and it is approximately related to the tensile strength of metals [38]. Vickers hardness evolution during the cladding tube manufacturing process is illustrated in Fig. 8(a). The hardness value increases dramatically from 253 ± 3 HV1 of the hot extruded tube to 308 ± 2 HV1 of 3rd cold pilgered tube. The hardness increases with increasing rolling passes is attributed to the formation of substructure during deformation, which can be verified in

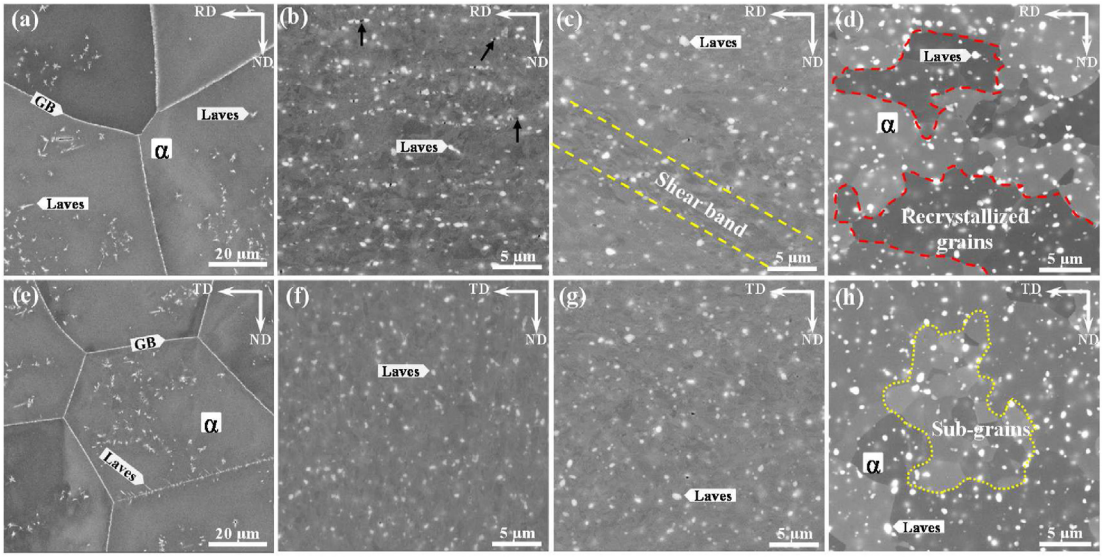

Fig. 7 – BSE images revealing the Laves phase particles evolution of tubes during pilgering step. (a,e) hot extruded, (b,f) 1st warm-pilgered, (c,g) 1st cold-pilgered and (d,h) after 1st cold-pilger annealed.

Table 4 – Statistical measures for number density and area fraction of Laves phase particles in different states of FeCrAl alloy tubes.

State	Number density (10^{11} m^{-2})	Area fraction (%)	Particle size (nm)
WR1 $_{RD-ND}$	9.73 ± 1.8	9.26 ± 1.9	310 ± 33
WR1$_{TD-ND}$	7.22 ± 2.4	7.47 ± 2.8	319 ± 31
WR2 $_{RD-ND}$	7.37 ± 0.4	7.42 ± 2.3	227 ± 18
WR2 $_{TD-ND}$	7.07 ± 0.3	6.87 ± 1.0	241 ± 14
WR2An $_{RD-ND}$	5.45 ± 0.6	6.46 ± 1.1	367 ± 27
WR2An $_{TD-ND}$	5.19 ± 0.4	6.62 ± 0.9	352 ± 24
CR1 $_{RD-ND}$	6.17 ± 0.2	5.72 ± 0.8	249 ± 20
CR1 $_{TD-ND}$	8.11 ± 0.2	5.68 ± 1.0	251 ± 14
CR1An $_{RD-ND}$	8.83 ± 0.2	6.39 ± 0.7	328 ± 16
CR1An $_{TD-ND}$	7.88 ± 0.3	6.56 ± 0.6	329 ± 20
CR3An $_{RD-ND}$	4.35 ± 0.1	6.25 ± 0.1	355 ± 29
CR3An $_{TD-ND}$	3.66 ± 0.1	4.73 ± 0.1	360 ± 32
CR3An $_{RD-TD}$	4.05 ± 0.2	4.98 ± 0.4	348 ± 27

Figs. 3(d) and 4(d). The annealing treatment resulted in a sharp drop of hardness, indicating that applied thermal treatment softens the ferritic structure. The hardness of the final annealed sample (CR3An) is ~210 HV1, corresponding to the fully recrystallized microstructure shown in Fig. 6. Fig. 8(b) display the tensile properties of FeCrAl alloy tubes after various rolling passes and annealing. The first warm pilger rolling resulted in an increase in yield strength from 565 MPa for the hot extruded tube to 759 MPa, but a sharp decrease in total elongation from 26.5% to 3.5%. After inter-pass annealing, the yield stress and ultimate tensile strength decreased (in agreement with the Vickers hardness results in Fig. 8(a)) and the total elongation increased, indicating that deformability was also restored. The final annealed cladding showed yield strength of 475 MPa and the highest total elongation of 41%.

To further illustrate the importance of inter-pass annealing for pilger rolling, Fig. 9 shows the tensile fracture morphologies of the first warm pilgered tube and after annealing. Obviously, many dimples can be seen in the fracture, and FeCrAl alloy tubes shows typical ductile fracture characteristics. Interestingly, the Laves phase particles are distributed in the dimples, as shown in the BSE mode in the upper half of Fig. 9. The secondary electron images displayed the fracture of the warm pilgered tube shows shallow dimples with a size below 2 μm, while the fractography after annealing shows deep and coarse dimples. It is worth noting that tear traces appeared in the dimple of the annealed tube, which is a typical feature of necking.

4.6. *Prediction of pilger rolling texture by VPSC model*

The crystallographic textures shown in the ODF maps in Figs. 2–4 indicated that the texture of FeCrAl alloy tubes significantly change during the pilgering. The evolution of rolling texture can usually be simulated by VPSC model. Based on the modeling in Section 3, we selected two representative steps, namely WR2 and CR1, to validate VPSC predictions. The texture of the WR1An and WR2An tubes as the initial texture to simulate the texture evolution after the WR2 and CR1 step. The VPSC predicted and experimentally measured textures during pilgering of FeCrAl tube after WR2 and CR1 steps are shown in Fig. 10. Fig. 10(a,c) show the experimentally measured $\varphi_2 = 45°$ ODF map after the WR2 and CR1 steps. Pilger rolling resulted in strong α-fiber, and the texture components {223}<110> and {111}<110> showed the highest orientation intensity. Regarding the ODF after the pilger rolling step (Fig. 10(b,d)), a good agreement between the measured ODF and the predicted ODF was observed. VPSC modeling has been shown to be suitable for predicting rolling texture development. However, some discrepancies between measured and predicted textures were found. The texture intensity of the experimental result is lower than that predicted in the VPSC simulations. This discrepancy may be due to some inherent limitations of the modeling, which assumes homogeneous macroscopic strain or ignores grain fragmentation. In addition, VPSC simulation is based on the microscopic texture imported by EBSD, which cannot consider the macroscopic texture of the whole sample. The precipitates were ignored in the simulation, although it influences the texture evolution.

5. Discussion

The microstructure, texture and precipitated phase are the key factors affecting the in-service performance of FeCrAl

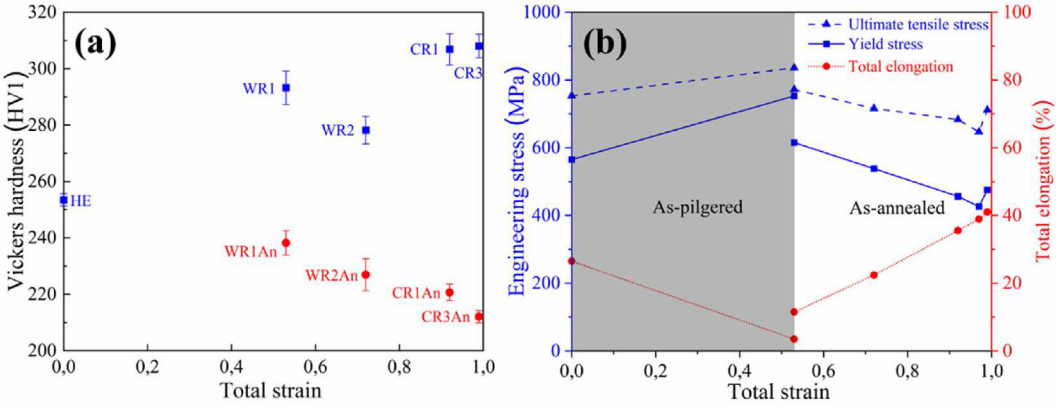

Fig. 8 – (a) Vickers hardness and (b) tensile properties of FeCrAl tubes after various processing steps.

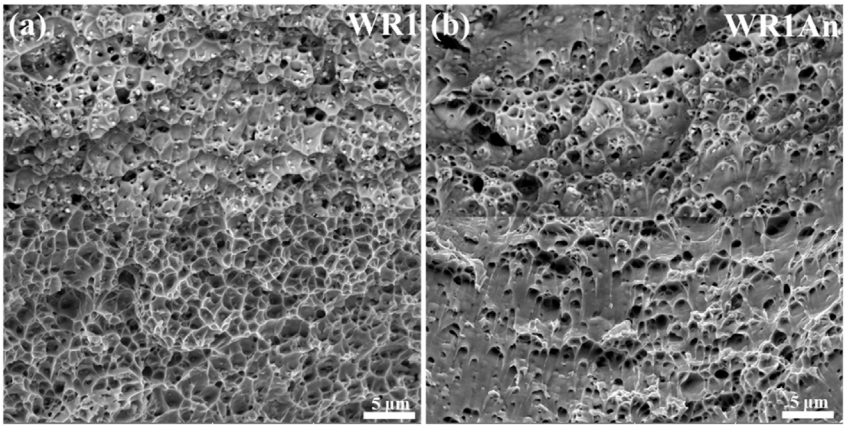

Fig. 9 – Tensile fracture morphologies of FeCrAl tubes (a) first warm pilger rolling and (b) after annealing.

cladding. The microstructure and texture evolution related to the TMP of FeCrAl cladding tube is of great value for industrial production.

5.1. *Microstructure controlled by processing conditions*

The present study provides a strong correlation between processing conditions and microstructure observed based on EBSD results. The microstructure is usually reflected by grain size, morphology, orientation, and grain boundary characteristics. The grain size and aspect ratio distribution for varying processing conditions are shown in Fig. 11. The equiaxed grain in the as-extruded microstructure is randomly distributed, ranging from 30 μm to 300 μm. Pilgering induced 'heterogeneous deformation' microstructure which the elongated larger grains were identified as 'non-fragmenting' and

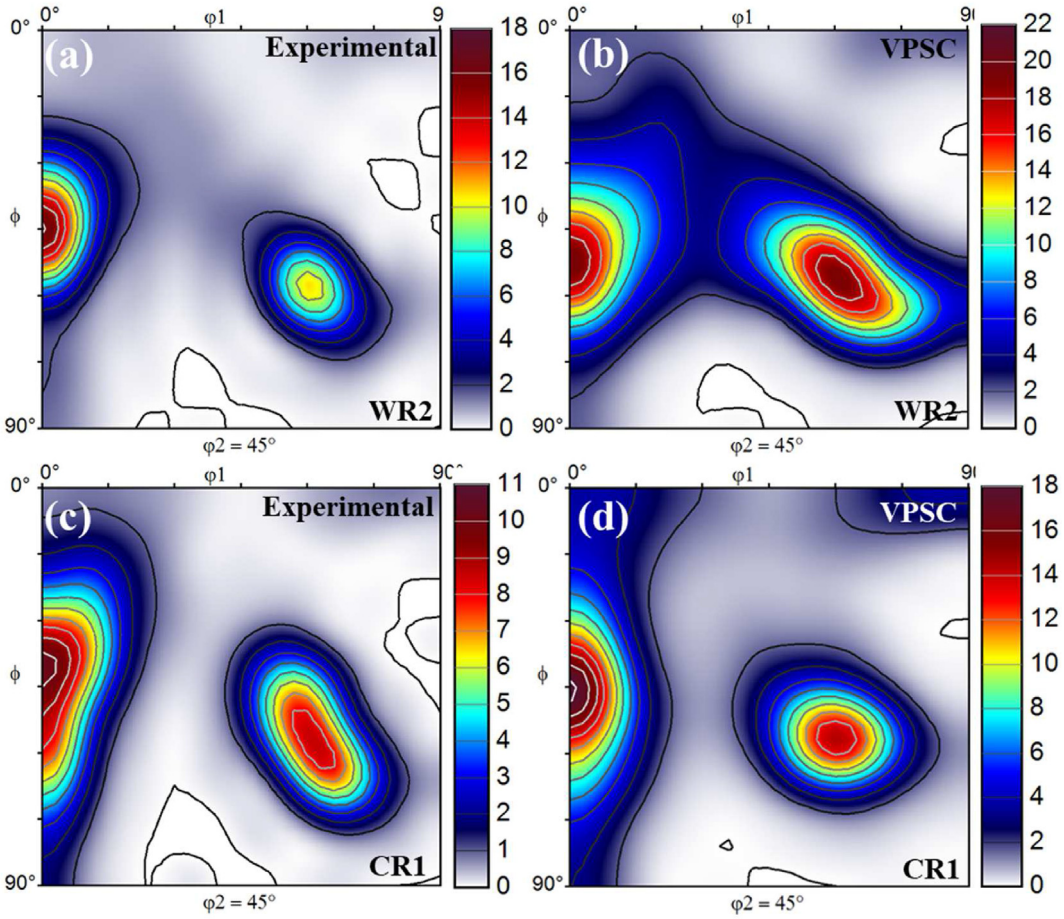

Fig. 10 – Experimental from EBSD and predicted from VPSC simulation $\varphi_2 = 45^\circ$ section ODF. (a,c) 2 nd warm pilgered and (b,d) 1st cold pilgered.

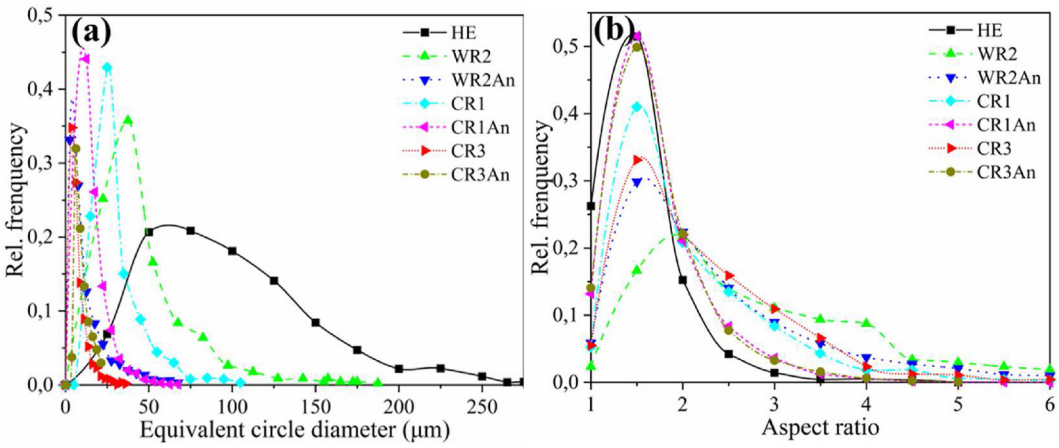

Fig. 11 – (a) Grain size and (b) aspect ratio distribution of tube during the pilgering and annealing process.

smaller grains generalized as 'fragmenting' undergo refinement in grain size (or grain fragmentation). Fig. 11(a) illustrates that pilgering results in grain refinement, but the aspect ratio is significantly increased as shown in Fig. 11(b). The WR2 sample showed the maximum average aspect ratio of 3.2. After the inter-pass annealing and final annealing, the elongated grain became almost equiaxed grain. It can be noted that the grain size and after the pilger cold rolling is almost equal, following Gaussian distribution. The 3rd pilger cold rolling and final annealing has little effect on grain refinement and aim to improve the dimensional accuracy of the tube and obtain a homogeneous microstructure.

Fig. 12 shows the misorientation distribution at representative stages in FeCrAl cladding tubes fabrication. Pilgering results in a significant increase in the frequency of LAGBs while inter-pass annealing increased the fraction of HAGBs. The reduced LAGBs and increased HAGBs during annealing are characteristic of recovery associated with recrystallization. In that scheme, LAGBs are progressively transformed into HAGBs with formation of new nuclei, which is consistent with Fig. 5(c). This recovery effect resulted in a decreasing hardness and an evolution of the grain morphology. In both HE and final annealed samples, the boundary misorientation angle distribution deviates from the Random distribution. Certain deviations from the Random distribution caused by the texture of the alloy could still be observed. A small fraction of LAGBs not accounted for by the Random distribution that is mainly caused by a small amount of deformed structure remaining in the microstructure as obvious from color variations in some of the grains in Figs. 1(a) and 6(a).

5.2. *Texture evolution during pilgering and annealing*

The crystallographic textures shown in ODF maps in Figs. 2–6 indicated that the texture of FeCrAl tubes significantly change during the pilgering and annealing. Based on Fig. 2(e), the hot extruded texture has strong α*-fiber and insignificant λ-fiber. It should be noted that λ-fiber oriented in <001> orientation with strong texture component {120}<001> while α*-fiber in the whole orientations decreases gradually with distance from {120}<001>. After pilgering, the overall texture intensity increases obviously, α*-fiber disappears and new α-fiber is formed. Pilgered samples exhibited typical rolling texture for BCC alloy consisting of α (<110>//RD) and γ (<111>//ND) fibers. These observations are in good agreement with reported cold deformed fibers of single phase FeCrAl alloys [18,19,39]. A crystalline rotation happens during cold deformation with <110> orientation or {111} plane as the rotation axis which is consistent with conventional ferritic steel [40]. Inter-pass annealing significantly affects texture evolution. The overall texture intensity of the WR2An sample decreased significantly, the α-fiber decreased while the partially recrystallized grains formed {001}<110> and {111}<110> components. The final annealing results in γ-fiber distributed throughout the orientation lines. This indicated that the γ-fiber belonging to recrystallized texture has better stability.

Fig. 13 Presents a quantitative estimation of the area fraction of three dominant fibers during fabricating FeCrAl cladding tube. Subset selection for each texture component was done at the maximum deviation of 15° from the ideal fiber orientations. The area fractions of three fibers of hot extruded tube are almost equal, implying a weak texture. As the pilger proceeding, the area fraction of α-fiber increases and λ-fiber decreases. The inter-pass annealing could additionally remove the α-fiber deformed grains due to the pilgering step and transform them into predominantly γ-fiber recrystallized grains. γ-fiber is known to have excellent formability, which explains the annealing restores the deformability of the tube. For FeCrAl alloys with bcc structure, the deformed grains and recrystallized grains are more likely to rotate along {110} slip plane or <111> slip direction. Therefore, the final finished tube has dominant α-fiber and γ-fiber. It is worth noting that the evolution is consistent in both longitudinal and cross-section planes of the tube, with the area fraction of the longitudinal plane being slightly higher than that of the cross-section plane.

5.3. *The effect of laves precipitates on microstructure*

The Laves phase particles in FeCrAl alloys are crucial to control the microstructure and improve high-temperature stability [18,25,28–32]. In order to illustrate the effect of the Laves phase on the microstructure, the warm pilgered tube was annealed at 800 °C for 1 h and 1100 °C for 1 h. Fig. 14 shows that

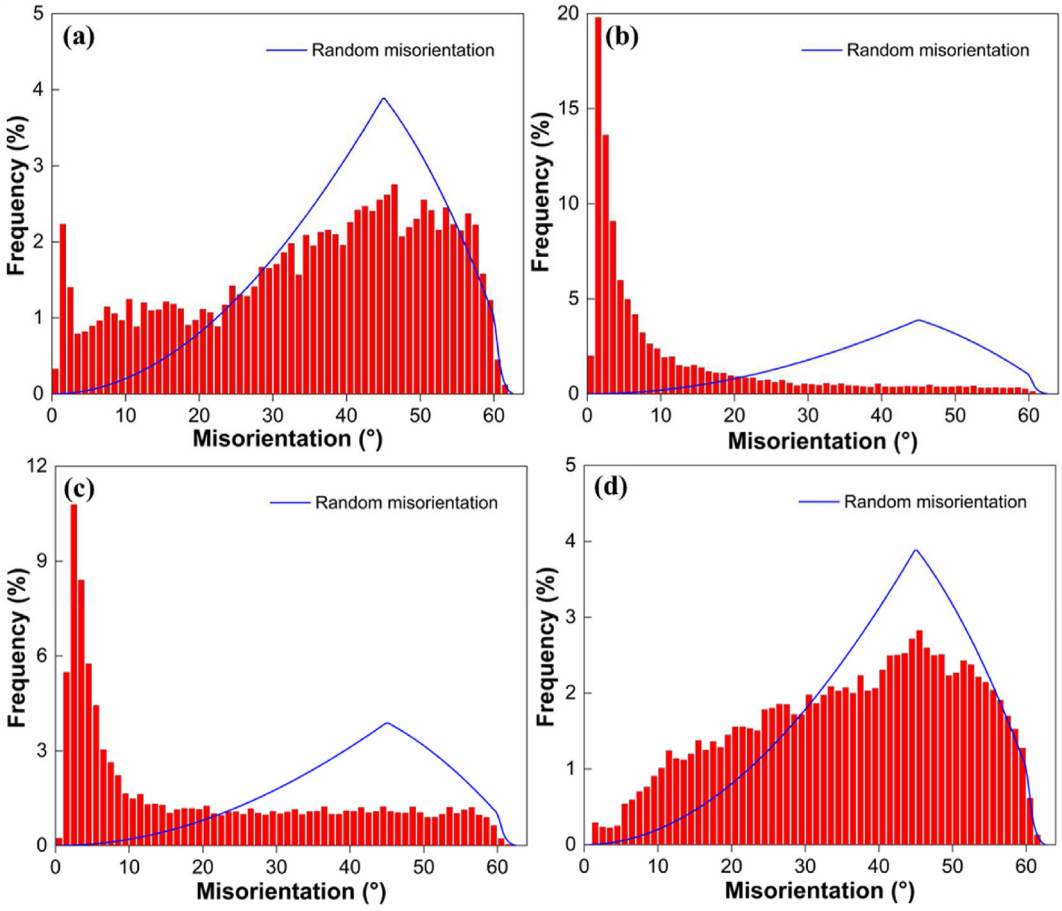

Fig. 12 – Misorientation distribution for representative conditions during fabrication of FeCrAl cladding tube including (a) As-extruded, (b) As-pilgered, (c) As-inter-pass annealed and (d) As-final annealed. Random distribution for untextured materials.

the microstructure is controlled by the Laves phase. The BSE image of Fig. 14(a) shows that the Laves precipitates pins grain or subgrain boundaries and control grain refinement. Fig. 14(a) EBSD-IQ map shows that these grains exhibit a bimodal structure with small size subgrains ~1 μm and large grains ~5 μm. It is worth noting that the IPF map from Fig. 14 shows

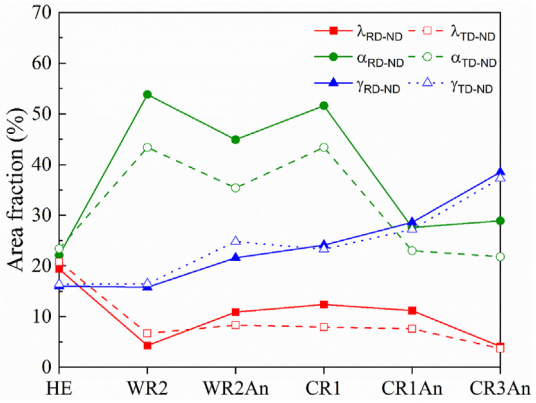

Fig. 13 – Area fraction of λ-fiber, α-fiber and γ-fiber changes during pilgering and annealing of FeCrAl tubes.

mixed microstructures consisting of recovered and recrystallized grains. The recovered area belonging to the γ-fiber with elongated dislocation cell bands ~10 μm in width were aligned to the RD, as indicated by high local misorientation as shown in Fig. 14(a) KAM map. The <100>//ND and <110>//ND orientated grains nucleated preferentially, belong recrystallized regions, showing low local misorientation. Once Laves precipitates dissolve into the matrix as shown in Fig. 14(a) BSE image, resulting in abnormally coarse grains. At high temperature, the ferrite matrix lacks the pinning of the Laves phase (solid solution into the matrix), resulting in significant grain coarsening. The abnormally coarse grains exhibit prominent γ-fiber at high temperature, indicating its high temperature stability. Therefore, these Laves phase dispersed in the matrix is very important to stabilize the microstructure at high temperature.

5.4. *Further development of FeCrAl alloy cladding*

The microstructural evolution of FeCrAl alloy tubes in the multi-pass pilgering process is closely related to the selected processing conditions, including the area reduction and Q value per pass and the inter-pass annealing time and temperature. In order to achieve desirable microstructures with

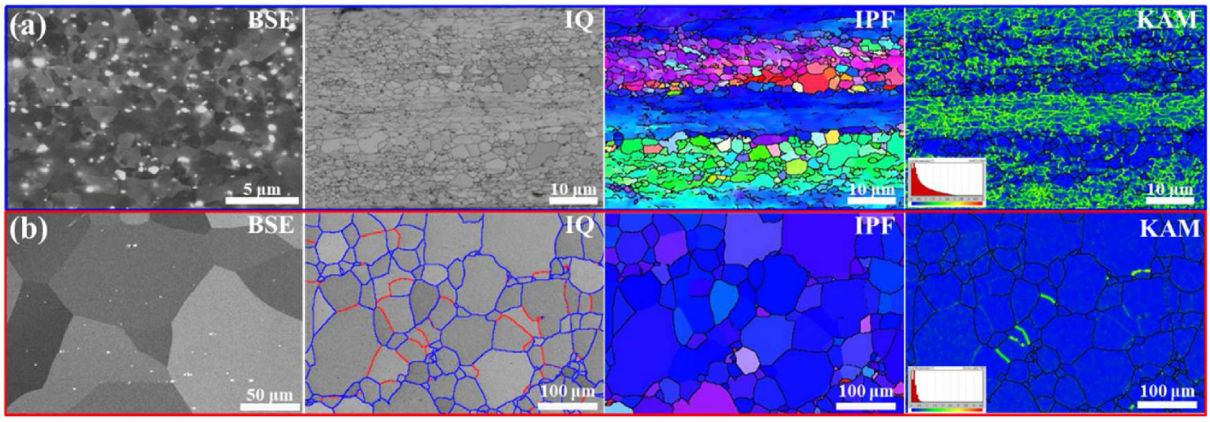

Fig. 14 – BSE images and EBSD results of the warm-pligered FeCrAl tube after annealing at (a) 800 °C for 1 h and (b) 1100 °C for 1 h

balanced processability and mechanical properties, processing conditions need to be optimized. In addition, high efficiency in industrial production requires less total passes to achieve final dimensions. A large strain per pass results in high cumulative stress. However, it is also likely to cause cracks or failure as the process progresses. Considering the typical tensile properties of the FeCrAl alloy tube in Fig. 8(b), the elongation is significantly reduced from 26.5% for the hot extruded tube to 3.5% after one pass of pilger rolling. At the same time, the yield strength and hardness increase significantly, implying that the resistance to deformation increased. The next pass of rolling without inter-pass annealing will inevitably cause cracking of the tube. Warm-pilger rolling and high annealing temperature is beneficial at the beginning of tube pilgering steps because it requires overcoming a relatively large deformation resistance of the initial wall thickness reduction. For practical tube fabrication, the inter-pass annealing time should be less than ~1 h and an appropriate annealing temperature to save energy and improve efficiency. The annealing temperature depends on the cumulative strain of the tube, and usually a high cumulative strain will reduce the recrystallization temperature. It can be seen from Table 2 and Fig. 5 that the low area reduction results in the tube still a large amount of deformed microstructure annealing at 850 °C for 1 h. However, the high area reduction results in a fully recrystallized microstructure of cold-pilger tube annealing at 800 °C for 1 h. Lower annealing temperatures are applied in the later stages of the tube pilgering step to control dimensional accuracy.

For single-phase bcc structure FeCrAl alloy tubes that cannot be strengthened by phase transformation, the thermomechanical processing process should be properly controlled. For the pilgering process, strain and Q value affect the microstructure and rolling texture. Inter-pass annealing softens the bcc matrix for further processing with refined grains and weak deformation texture. Therefore, inter-pass annealing is very important for the subsequent processing of cladding. In addition, the addition of chemical components of FeCrAl alloys such as Mo, Nb, will form Laves phases to effectively strengthen and delay the recrystallization kinetics of the alloy compared with the base components. Hence, the effect of the chemical composition should also be considered to develop FeCrAl alloy cladding.

6. Conclusions

The microstructure and texture evolutions of industrially fabricated FeCrAl cladding tubes were investigated with the help of EBSD and SEM. The main conclusions are as follows.

1. The hot extruded microstructure exhibited ~100 μm equiaxed <001> orientated grains while pilger rolling changes to elongated and fragmented grains with <111> and <110> orientations. The applied annealing treatment restores the deformed grain with high stored energy to fine recrystallized grains. Final annealed tube showing ~11 μm recrystallized grains with preferred <111> orientation in 3D directions.
2. Textural evolution during the fabrication of FeCrAl cladding was generalized as the evolution of α-fiber and γ-fibers. The pilgered texture predicted by VPSC is consistent with the experimental results. Pilgering strengthened α-fiber, while annealing weakened α-fiber and strengthened γ-fiber.
3. Pilger rolling results in increases in hardness and strength, but a sharp decrease in elongation. Inter-pass annealing softens the ferritic matrix and restores ductility. The final annealed cladding applied with TMP has fine grains with total elongation of ~41% and yield strength of 475 MPa.
4. Microstructural evolution in the Laves precipitates followed the sequence of faceted needle-like → spherical → faceted ellipsoidal in pilger processing FeCrAl cladding tubes. Fabrication of the cladding by TMP halved the area fraction and number density of the Laves phase. Annealing results in coarsening and resolution of Laves precipitates. Laves precipitates could pin the grain boundaries to suppress grain coarsening.

Declaration of competing interest

The authors declare that they have no known competing financial interests or personal relationships that could have appeared to influence the work reported in this paper.

Acknowledgments

The authors would like to thank the Key Project of Nuclear Safety and Advanced Nuclear Technology, China for providing the funding (Grant No: 2019YFB1901002) to carry out this work.

REFERENCES

[1] Yamamoto Y, Pint BA, Terrani KA, Field KG, Yang Y, Snead LL. Development and property evaluation of nuclear grade wrought FeCrAl fuel cladding for light water reactors. J Nucl Mater 2015;467:703–16. https://doi.org/10.1016/j.jnucmat.2015.10.019.

[2] Rebak RB. Chapter 5 – FeCrAl–iron–chromium–aluminum monolithic alloys, accident tolerant materials for Light water reactor fuels. Elsevier; 2020. p. 83–141. https://doi.org/10.1016/B978-0-12-817503-3.00005-5.

[3] Terrani KA. Accident tolerant fuel cladding development: promise, status, and challenges. J Nucl Mater 2018;501:13–30. https://doi.org/10.1016/j.jnucmat.2017.12.043.

[4] Pint BA, Terrani KA, Brady MP, Cheng T, Keiser JR. High temperature oxidation of fuel cladding candidate materials in steam–hydrogen environments. J Nucl Mater 2013;440(1–3):420–7. https://doi.org/10.1016/j.jnucmat.2013.05.047.

[5] Lee CM, Jeong HY, Yoon A, Mok YK, Sohn DS. Microstructural analysis of preformed oxides on a zirconium alloy before and after subsequent oxidation at 1000–1200° C. Corrosion Sci 2018;139:410–20. https://doi.org/10.1016/j.corsci.2018.05.022.

[6] Raiman SS, Field KG, Rebak RB, Yamamoto Y, Terrani KA. Hydrothermal corrosion of 2nd generation FeCrAl alloys for accident tolerant fuel cladding. J Nucl Mater 2020;536:152221. https://doi.org/10.1016/j.jnucmat.2020.152221.

[7] Yin L, Jurewicz TB, Larsen M, Drobnjak M, Graff CC, Lutz DR, et al. Uniform corrosion of FeCrAl cladding tubing for accident tolerant fuels in light water reactors. J Nucl Mater 2021;554:153090. https://doi.org/10.1016/j.jnucmat.2021.153090.

[8] Dong JP, Kim HG, Park JY, Yang IJ, Park JH, Yang HK. A study of the oxidation of FeCrAl alloy in pressurized water and high-temperature steam environment. Corrosion Sci 2015;94:459–65. https://doi.org/10.1016/j.corsci.2015.02.027.

[9] Abe H, Furugen M. Method of evaluating workability in cold pilgering of zirconium alloy tube. Mater Trans 2010;51(7):1200–5. https://doi.org/10.2320/matertrans.P-M2010812.

[10] Lemaignan C. 2.07-Zirconium alloys: properties and characteristics. In: Comprehensive nuclear materials. Oxford: Elsevier; 2012. p. 217–32. https://doi.org/10.1016/B978-0-08-056033-5.00015-X.

[11] Gussev MN, Field KG, Yamamoto Y. Design, properties, and weldability of advanced oxidation-resistant FeCrAl alloys. Mater Des 2017;129:227–38. https://doi.org/10.1016/j.matdes.2017.05.009.

[12] Herrmann J, Inden G, Sauthoff G. Deformation behaviour of iron-rich iron- aluminum alloys at low temperatures. Acta Mater 2003;51:2847–57. https://doi.org/10.1016/S1359-6454(03)00089-2.

[13] Qu HP, Lang YP, Yao CF, Chen HT, Yang CQ. The effect of heat treatment on recrystallized microstructure, precipitation and ductility of hot-rolled Fe–Cr–Al–REM ferritic stainless steel sheets. Mater Sci Eng 2013;562:9–16. https://doi.org/10.1016/j.msea.2012.11.008.

[14] Yamamoto Y, Sun Z, Pint BA, Terrani KA. Optimized gen-II FeCrAl cladding production in large quantity for campaign testing. Oak Ridge: Oak Ridge National Laboratory; 2016.

[15] Sun Z, Yamamoto Y. Processability evaluation of a Mo-containing FeCrAl alloy for seamless thin-wall tube fabrication. Mater Sci Eng 2017;700:554–61. https://doi.org/10.1016/j.msea.2017.06.036.

[16] Osika J, Palkowski H, Świątkowski K, Pociecha D, Kula A. Analysis of material deformation during the new cold tube rolling process realized on the new generation of pilger mills. Arch Metall Mater 2009;54(4):1239–51.

[17] Yagiz A. Modeling of cold pilgering of tubes. Luleå University of Technology: Licentiate Thesis; 2017. https://doi.org/10.13140/RG.2.2.33505.15202.

[18] Zhang Y, Wang H, Sun H, Chen G. Effects of annealing temperature on the microstructure, textures and tensile properties of cold-rolled Fe–13Cr–4Al alloys with different Nb contents. Mater Sci Eng 2020;798:140236. https://doi.org/10.1016/j.msea.2020.140236.

[19] Liang XL, Wang H, Pan QF, Zheng JY, Liu HQ, Zhang RQ, et al. Recrystallization and mechanical properties of cold-rolled FeCrAl alloy during annealing. J Iron Steel Res Int 2020;27:549–65. https://doi.org/10.1007/s42243-020-00387-z.

[20] Sun Z, Bei H, Yamamoto Y. Microstructural control of FeCrAl alloys using Mo and Nb additions. Mater Char 2017;132:126–31. https://doi.org/10.1016/j.matchar.2017.08.008.

[21] Bakhsheshi-Rad HR, Haerian B, Najafizadeh A, Idris MH, Kadir MRA, Hamzah E, et al. Cold deformation and heat treatment influence on the microstructures and corrosion behavior of AISI 304 stainless steel. Can Metall Q 2013;52(4):449–57. https://doi.org/10.1179/1879139513Y.0000000101.

[22] Badkoobeh F, Mostaan H, Rafiei M, Bakhsheshi-Rad HR, Berto F. Microstructural characteristics and strengthening mechanisms of ferritic–martensitic dual-phase steels: a review. Metals 2022;12(1):101. https://doi.org/10.3390/met12010101.

[23] Garmeh B, Kasiri-Asgarani M, Amini K, Ghayour H, Bakhsheshi-Rad HR, Berto F. Effect of vanadium and rare earth on the structure, phase transformation kinetics and mechanical properties of carbide-free bainitic steel containing silicon. Appl Sci 2022;12(3):1668. https://doi.org/10.3390/app12031668.

[24] Huang S, Dolley E, An K, Yu D, Crawford C, Othon M, et al. Microstructure and tensile behavior of powder metallurgy FeCrAl accident tolerant fuel cladding. J Nucl Mater 2022:153524. https://doi.org/10.1016/j.jnucmat.2022.153524.

[25] Sun H, Wang H, He X, Wang F, An X, Wang Z. Study on high temperature creep behavior of the accident-resistant cladding Fe-13Cr-4Al-1.85Mo-0.85Nb alloy. Mater Sci Eng 2021;802:140688. https://doi.org/10.1016/j.msea.2020.140688.

[26] Yang Z, Wang ZX, Xia CH, Ouyang MH, Peng JC, Zhang HW, et al. Aluminum suppression of α′ precipitate in model Fe–Cr–Al alloys during long-term aging at 475° C. Mater Sci Eng 2020;772:138714. https://doi.org/10.1016/j.msea.2019.138714.

[27] Briggs SA, Edmondson PD, Littrell KC, Yamamoto Y, Howard RH, Daily CR, et al. A combined APT and SANS investigation of α′ phase precipitation in neutron-irradiated

model FeCrAl alloys. Acta Mater 2017;129:217–28. https://doi.org/10.1016/j.actamat.2017.02.077.
[28] Sun Z, Edmondson PD, Yamamoto Y. Effects of Laves phase particles on recovery and recrystallization behaviors of Nb-containing FeCrAl alloys. Acta Mater 2017;144:716–27. https://doi.org/10.1016/j.actamat.2017.11.027.
[29] Barrilao JL, Kuhn B, Wessel E. Identification, size classification and evolution of Laves phase precipitates in high chromium, fully ferritic steels. Micron 2017;101:221–31. https://doi.org/10.1016/j.micron.2017.07.010.
[30] Chai YW, Kato K, Yabu C, Ishikawa S, Kimura Y. Disconnections and Laves (C14) precipitation in high-Cr ferritic stainless steels. Acta Mater 2020;198:230–41. https://doi.org/10.1016/j.actamat.2020.08.006.
[31] Chen L, Wang H, An X, Huang X. Recovery, recrystallization and precipitation behavior in an ATF FeCrAl alloy during annealing treatment. Mater Char 2022;190:112026. https://doi.org/10.1016/j.matchar.2022.11.2026.
[32] Ikeda K, Yamoah NKG, Reynolds Jr WT, Hamada J, Murayama M. Effect of Laves phase on high-temperature deformation and microstructure evolution in an 18Cr-2Mo-0.5Nb ferritic stainless steel. Metall Mater Trans A 2015;46:3460–9. https://doi.org/10.1007/s11661-015-2936-y.
[33] Tome C, Lebensohn R. Material modeling with the visco-plastic self-consistent (VPSC) approach: theory and practical applications. Elsevier; 2023.
[34] Tomé CN, Lebensohn RA. Manual for VPSC7d. Los Alamos: Los Alamos National Laboratory; 2012. https://icme.hpc.msstate.edu/mediawiki/images/8/80/VPSC7d_manual.pdf.
[35] Aghamiri SMS, Sowa T, Ukai S, Oono N, Sakamoto K, Yamashita S. Microstructure and texture evolution and ring-tensile properties of recrystallized FeCrAl ODS cladding tubes. Mater Sci Eng 2020;771:138636. https://doi.org/10.1016/j.msea.2019.138636.
[36] Girard E, Guillen R, Weisbecker P, François M. Effect of plastic shearing on damage and texture on Zircaloy-4 cladding tubes: experimental and numerical study. J Nucl Mater 2001;294:330–8. https://doi.org/10.1016/S0022-3115(00)00729-7.
[37] Choi SH, Jin YS. Evaluation of stored energy in cold-rolled steels from EBSD data. Mater Sci Eng 2004;371:149–59. https://doi.org/10.1016/j.msea.2003.11.034.
[38] Zhang P, Li SX, Zhang ZF. General relationship between strength and hardness. Mater Sci Eng 2011;529:62–73. https://doi.org/10.1016/j.msea.2011.08.061.
[39] Qin X, Zhang R, Du P, Pei J, Pan Q, Cao Y, et al. Recrystallization and texture evolution of cold pilgered FeCrAl cladding tube during annealing at 700° C~ 1000° C. J Nucl Mater 2023;577:154303. https://doi.org/10.1016/j.jnucmat.2023.154303.
[40] Humphreys J, Rohrer GS, Rollett A. Recrystallization and related annealing phenomena. 3rd. ed. Elsevier; 2017.